# Taylor & Francis Taylor & Francis Group

# **Aerosol Science and Technology**

ISSN: (Print) (Online) Journal homepage: https://www.tandfonline.com/loi/uast20

Detection of sub-5nm naturally charged carbonaceous materials from a sooting laminar premixed flame by a water condensation Particle Counter (WCPC) enhanced by a Di-Ethylene Glycol (DEG) saturator inlet

Farnaz Khosravi, Gregory S. Lewis, Michel Attoui, Arantza Eiguren-Fernandez & Francesco Carbone

**To cite this article:** Farnaz Khosravi, Gregory S. Lewis, Michel Attoui, Arantza Eiguren-Fernandez & Francesco Carbone (2023) Detection of sub-5nm naturally charged carbonaceous materials from a sooting laminar premixed flame by a water condensation Particle Counter (WCPC) enhanced by a Di-Ethylene Glycol (DEG) saturator inlet, Aerosol Science and Technology, 57:11, 1069-1086, DOI: 10.1080/02786826.2023.2247458

To link to this article: <a href="https://doi.org/10.1080/02786826.2023.2247458">https://doi.org/10.1080/02786826.2023.2247458</a>

	Published online: 07 Sep 2023.
	Submit your article to this journal $ {f Z} $
ılıl	Article views: 54
ď	View related articles ☑
CrossMark	View Crossmark data ☑







# Detection of sub-5nm naturally charged carbonaceous materials from a sooting laminar premixed flame by a water condensation Particle Counter (WCPC) enhanced by a Di-Ethylene Glycol (DEG) saturator inlet

Farnaz Khosravi<sup>a</sup>, Gregory S. Lewis<sup>b</sup>, Michel Attoui<sup>c</sup>, Arantza Eiguren-Fernandez<sup>b</sup>, and Francesco Carbone<sup>a</sup>

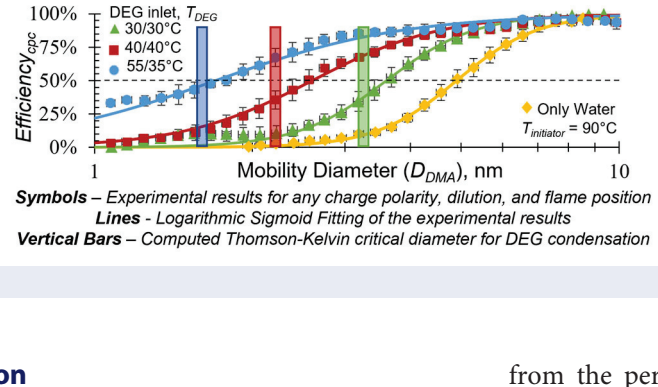
<sup>a</sup>Department of Mechanical Engineering, University of Connecticut, Storrs, Connecticut, USA; <sup>b</sup>Aerosol Dynamics, Berkeley, California, USA; <sup>c</sup>Universite Paris Est Creteil and Universite de Paris, CNRS, LISA, Creteil, France

#### **ABSTRACT**

Combustion is one of the major contributors to air pollution and Condensation Particle Counters (CPCs) provide effective monitoring of atmospheric aerosols since they can detect both charged and neutral materials in low number concentrations. The detection efficiency of any CPC for materials smaller than 5 nm requires ad-hoc calibrations because it is affected by the analyte's size, shape, charge state, composition, and wettability by the condensing fluid. This study characterizes a Water-based CPC (WCPC) prototype for the detection of the naturally charged carbonaceous products of an incipiently sooting laminar premixed flame. The WCPC can activate condensation growth and (50% efficient) detection of hydrophobic flame-formed carbonaceous materials naturally charged in positive and negative polarities with mobility diameters as small as 4.3 nm and 4.8 nm, respectively. The addition of a simple Di-Ethylene Glycol (DEG) saturator inlet enhances the 50% detection cutoff to mobility diameters as small as 1.8 nm or 1.6 nm for materials charged in positive or negative polarity, respectively. The coupling of the DEG saturator inlet to the WCPC creates a new DEG-WCPC instrument able to detect efficiently both hydrophobic and hydrophilic sub-5nm aerosols with a marginal increase in manufacturing cost (<10%), dimensions, and weight (<0.25 kg).

# **GRAPHICAL ABSTRACT**

100%



#### **ARTICLE HISTORY**

Received 25 April 2023 Accepted 30 July 2023

#### **EDITOR**

Jingkun Jiang

#### 1. Introduction

Air pollution by aerosols is one of the major environmental concerns in recent years (Manisalidis et al. 2020), and its monitoring, control, and regulation are the main inspiration for the improvement of particle counting/detecting technologies Kulkarni, Baron, and Willeke 2011). Among atmospheric aerosols, nanosized combustion-generated materials are prevalent in urban areas (Rönkkö and influence Timonen 2019), climate change (Schraufnagel 2020), and are the most worrisome

from the perspective of their health effects, given the enhancement in toxicity reported for particles of increasingly smaller sizes (Lighty, Veranth, and Sarofim 2000; Oberdörster, Oberdörster, Oberdörster 2005; Nel et al. 2006; Pedata et al. 2015; Hewitt, Chappell, and Powell 2020; Moreno-Ríos, Tejeda-Benítez, and Bustillo-Lecompte 2022). As a result, there is a need for developing instruments able to detect ever-smaller combustion-generated materials at ever-lower concentration levels not only to study the mechanisms of soot nucleation in flames (Smyth et al. 1985; Basile et al. 2002; Bockhorn, D'Anna, and Sarofim 2009; D'Anna 2009; Wang 2011; Carbone, Attoui, and Gomez 2016; Carbone, Gleason, and Gomez 2017; Carbone, Moslih, and Gomez 2017; Carbone et al. 2019, 2021; Johansson et al. 2018; Commodo et al. 2019; Schulz et al. 2019; Rundel et al. 2022) but also to monitor their fate in the atmosphere.

From the perspective of measuring aerosols smaller than 10 nm, Condensation Particle Counters (CPCs) benefit from several features compared to other diagnostics. They are relatively affordable to purchase and operate, are lightweight and small, and have modest electric power consumption so that they are easily and broadly usable for field and altitude studies (e.g., McMurry 2000; Cheng 2011; Kangasluoma and Attoui 2019). They benefit from high sensitivity and large dynamic range being able to detect particle concentrations from a few cm<sup>-3</sup> to more than 10<sup>5</sup> cm<sup>-3</sup> (Lewis and Hering 2013; Avula et al. 2021). Most importantly, CPCs enable the detection of both charged and uncharged materials (Seto et al. 1997; Winkler et al. 2008) with sizes above a threshold value settable upon adjusting the operating parameters. Therefore, CPCs can be used also for aerosol sizing (Sipilä et al. 2008; Barmpounis et al. 2018; Picard, Attoui, and Sellegri 2019) or fundamental condensation studies (Riipinen et al. 2009; Kuldinow et al. 2022; Attoui et al. 2023).

In a CPC, a working fluid is vaporized and dispersed in the aerosol to be analyzed while temperature conditioning of the flow is implemented to achieve supersaturation so that a fraction of the particles can grow via condensation to sizes large enough for counting them via laser light scattering (McMurry 2000; Gamero-Castaño and Fernandez de La Mora 2000; Sgro and Fernandez de la Mora 2004; Cheng 2011; Jiang et al. 2011; Kuang et al. 2012; Vanhanen et al. 2011; Kangasluoma et al. 2014; Lehtipalo et al. 2014; Hering et al. 2017; Attoui 2018; Wlasits et al. 2020). In laminar flow CPCs, as the one investigated herein, the dispersion of the condensing vapor and the achievement of supersaturation are implemented via the diffusive transport of species and heat. Alternatively, turbulent mixing CPCs have been used somewhat more broadly for the detection of sub-3nm aerosols (Gamero-Castaño and Fernandez de La Mora 2000; Sgro and Fernandez de la Mora 2004; Vanhanen et al. 2011; Kangasluoma et al. 2014; Lehtipalo et al. 2014).

Regardless of how supersaturation is achieved, condensation growth is activated without an energy barrier on condensation nuclei larger than a critical size, primarily because of the Kelvin effect (Friedlander 2000; Hinds 1999; Seinfeld and Pandis 2016). The critical size is influenced also by the condensation nuclei's charge (Thomson 1903; Seto et al. 1997; Winkler et al. 2008), shape, and wettability by the condensing fluid (Fletcher 1958; Fernandez de la Mora 2011; Wlasits et al. 2020; Kuldinow et al. 2022). As a result, the detection efficiency of a CPC (i.e., the fraction of the condensation nuclei being counted) as a function of size and charge state is related not only to the CPC's specific design but also to the properties of the analytes and the working fluid (Kangasluoma and Attoui 2019; Kuang et al. 2012; Wlasits et al. 2020). Although isopropanol has widespread applications (TSI 2023), the working fluids used most commonly in CPCs able to detect sub-10nm aerosols are n-butanol (Iida, Stolzenburg, and McMurry 2009; Brilke et al. 2020; Sharma et al. 2021) and water (Hering and Stolzenburg 2005; Iida et al. 2008). In theory, Waterbased CPCs (WCPCs) can detect extremely small materials thanks to the high surface tension of water, but their detection efficiency is more sensitive to the analyte composition and charge state (Hering et al. 2017) compared to that of n-butanol-based ones (Attoui 2018; Sharma et al. 2021). Indeed, most aerosols abundant in urban areas, including carbonaceous ones, are more wettable by alcohols than water. The use of bio-compatible water is also advisable compared to n-butanol because the grown nuclei can be collected directly and concentrated for ensuing toxicological studies (Eiguren-Fernandez, Kreisberg, and Hering 2017). The technical advantages and shortcomings of a broad variety of condensing fluids have been considered in the literature (Iida, Stolzenburg, and McMurry 2009) but the development of devices has been limited only to a few options. A literature review of many nontoxic fluids other than water (Iida, Stolzenburg, and McMurry 2009) pointed to Diethylene glycol (DEG) as one of the best fluids to activate the condensation growth of the smallest clusters. As a drawback, DEG condensation may be sensitive to the analyte composition (i.e., its wettability by DEG) and, importantly in the context of this study, only grows the droplets to about 100 nm (Winkler et al. 2008; Vanhanen et al. 2011; Lehtipalo et al. 2014; Ahonen et al. 2017), which is too small for easy optical counting. Typically DEG-based devices are followed by a second conventional n-Butanol CPC to grow the smallest clusters to detectable sizes (Kuang et al. 2012; Vanhanen et al. 2011; Lehtipalo et al. 2014; Hering et al. 2017; Ahonen et al. 2017; Attoui 2018; Kangasluoma and Attoui 2019).

Lastly, diffusion losses which occur before the condensation nuclei grow large enough to hinder their Brownian motion, also influence the CPCs' detection efficiency. As a result, the detection efficiency of a specific CPC design for several values of its operating parameters is difficult to be predicted from first principles and requires (charge state- and material-dependent) ad-hoc calibrations.

The first version of a WCPC introduced by Hering and Stolzenburg (2005) consists of two temperature-controlled tubular stages of a growth tube with water-wetted wick walls. A laminar aerosol flow is cooled in the first (conditioner) stage and heated and humidified in the second (initiator) stage. Supersaturation is established in the initiator because the gas mixture thermal diffusivity is smaller than the molecular diffusivity of water (i.e., the water vapor Lewis number is smaller than 1). Recently, Hering, Spielman, and Lewis (2014) and Hering et al. (2019) improved the two-stage design by adding a third cold "moderator" stage. The moderator lowers the temperature and dew point of the flow exiting the growth tube while sustaining its supersaturation. As a result, it minimizes water consumption, while avoiding both overheating and water condensation in the optical counter and subsequent flow path. Importantly, the moderator enables the use of temperature differences between the conditioner and the initiator as high as 99°C (i.e., the highest achievable supersaturations) to activate the growth of the smallest possible condensation nuclei.

As mentioned above, the detection efficiency of any CPC needs to be calibrated for specific materials and WCPCs have not been characterized for the detection of the smallest flame-formed carbonaceous materials. This study aims at characterizing the detection efficiency of a WCPC prototype (ADI-2021-1, Aerosol Dynamics Inc.), operated under several operating conditions, for diluted aerosols extracted directly from an incipiently sooting premixed flame of ethylene/air that has been extensively characterized in the literature (Carbone, Attoui, and Gomez 2016; Carbone, Gleason, and Gomez 2017; Carbone, Moslih, and Gomez 2017; Carbone et al. 2019, 2021). Additionally, calibrations have been performed also upon installing a simple DEG saturator inlet consisting of a tubular DEG wetted wick whose operation concept is somewhat similar to that described by Flagan, Kaufman, and Sem (2005). Nonetheless in other existing DEG-based instruments, the flow is passed sequentially through a hot saturator and a cold condenser which grows the condensation nuclei to about 100 nm before they can be counted by a separate CPC. In the DEG-WCPC resulting from the installation of the DEG saturator inlet to the WCPC, the first conditioner stage of the WCPC acts also as a final DEG condenser stage, resulting

in one of the simplest imaginable designs for a CPC relying on two separate condensing fluids.

## 2. Methods

The experimental system consists of several components. A laminar premixed flame generates carbonaceous materials including incipient soot particles, molecular clusters, and gaseous soot precursors all of which have been characterized extensively in the literature (Carbone, Attoui, and Gomez 2016; Carbone, Gleason, and Gomez 2017; Carbone, Moslih, and Gomez 2017; Carbone et al. 2019, 2021). A horizontal-tube probe, crossed by pure nitrogen, is used to sample and dilute the naturally charged flame products (Carbone, Attoui, and Gomez 2016; Carbone et al. 2019) while conveying them to the inlet slit of a Half-Mini High-Resolution Differential Mobility Analyzer (HR-DMA) (Fernandez de la Mora and Kozlowski 2013; Fernandez de la Mora 2017). The DMA classifies the aerosolized materials with the desired mobility diameter  $(D_{DMA})$  (Larriba-Andaluz and Carbone 2021) selected in the 1-10 nm interval via a control voltage  $(V_{DMA})$ . The prevalently monodisperse charged materials exiting the HR-DMA are detected by a low noise calibrated Faraday Cup Electrometer (FCE, model PR-BLK-255, Amperical Industries) of the type described in (Fernandez de la Mora et al. 2017), and the ADI-2021-1 WCPC prototype (with or without the DEG saturator inlet), connected in parallel to the DMA outlet. The efficiency of the (DEG-) WCPC in detecting naturally charged flame-generated materials, extracted under different sampling conditions, is determined by stepping  $V_{DMA}$  and comparing the (DEG-) WCPC and FCE readings. A schematic of the experimental system is depicted in Figure 1 and a detailed description of its main components follows below.

## 2.1. Flame and dilution sampling

The source of carbonaceous aerosols for this study is a laminar premixed flame of ethylene/air with a C/O ratio of 0.69 and a cold gas velocity of 58.7 mm/s stabilized on a honeycomb burner (Carbone, Gleason, and Gomez 2017; Carbone, Moslih, and Gomez 2017). The flame is shielded from the surrounding air by 35 lpm of shroud nitrogen, flown through a dedicated annulus (ID = 48 mm, OD = 72 mm) of the burner's stainless-steel honeycomb, while a brass plate (OD = 48 mm), installed at a Height Above the Burner (HAB) of 40 mm, suppresses any flame flickering.

A stainless-steel tube (OD =  $6.35 \,\mathrm{mm}$ ,  $305 \,\mathrm{mm}$  long, and 0.127 mm wall thickness) probe is equipped with an

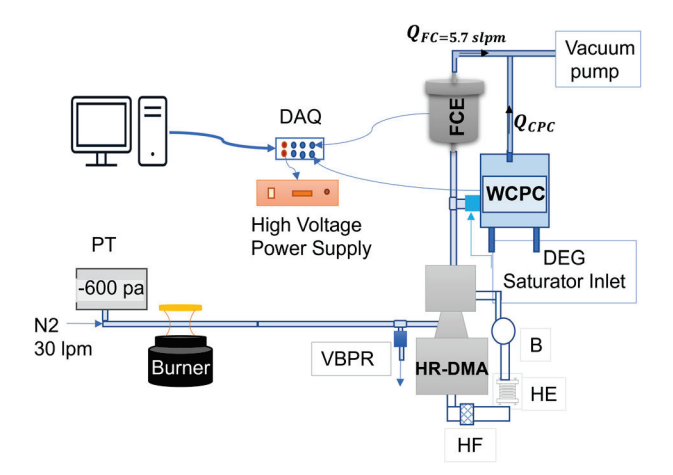


**Figure 1.** Schematic of the experimental system. List of components: WCPC- Water-based CPC ADI-2021-1 prototype with optional DEG saturator inlet, FCE – Faraday Cup Electrometer, DAQ – Data AcQuisition Board, HR-DMA – Half Mini High-Resolution Differential Mobility Analyzer, B – Blower, HE -Heat Exchanger, HF – HEPA Filter, PT – Pressure Transducer, VBPR -Vacuum Back Pressure Regulator.

orifice drilled in its wall which faces the burner outlet to sample the flame products at either HAB =  $7.5 \,\mathrm{mm}$  or HAB = 10 mm (Carbone, Attoui, and Gomez 2016; Carbone et al. 2019). The sampled flow is diluted quickly into 30 lpm of pure nitrogen steadily crossing the probe tube. Dilution minimizes coagulation of the analytes during the 47 ms necessary to transport the flame products from the sampling orifice to the HR-DMA inlet slit. The sampling velocity and flame perturbation is kept constant in all experiments by using a constant suction pressure in the probe of about 600 Pa (Carbone, Moslih, and Gomez 2017). Experiments are repeated by either up- or downstepping  $V_{D\!M\!A}$  and upon applying a Dilution Ratio (DR) of 355 or 700 when using the 0.36 mm or 0.25 mm probing orifice, respectively (Carbone, Attoui, and Gomez 2016; Carbone, Moslih, and Gomez 2017). The repeated experiments assess not only the results' uncertainty but also if sample coagulation and aging at high temperatures in the flame or low temperatures in the probe affect the WCPC detection efficiency in the  $D_{DMA}$  interval between 1 nm and 10 nm.

# 2.2. High-Resolution Differential Mobility Analysis (HR-DMA)

A fraction of the diluted sample enters the classification section through the inlet slit on the electrically grounded HR-DMA external electrode with the flow rate  $Q_{DMA} \leq Q_{FCE} + Q_{CPC}$ , where  $Q_{FCE}$  and  $Q_{CPC}$  are extracted at the outlet of the FCE and WCPC, respectively. The inequality is due to water evaporation within the WCPC which causes the flow entering the WCPC to be smaller than

the  $Q_{CPC}$  monitored at the WCPC outlet.  $Q_{FCE}$  and  $Q_{CPC}$  are kept constant during measurements, in most cases to  $Q_{FCE}=5.7$  slpm and  $Q_{CPC}=0.33$  lpm except when investigating the effect of using different  $Q_{CPC}$  on the results. The aerosol enters the L=20 mm long cylindrical classification section between the HR-DMA coaxial electrodes whose radiuses are  $R_{in}=4$  mm and  $R_{out}=7$  mm, respectively. When  $V_{DMA}$  is applied between the electrodes,  $Q_{DMA}$  exits the outlet slit on the HR-DMA internal electrode, deprived of all charged materials but those with polarity opposite to  $V_{DMA}$  and whose electrical mobility, Z, satisfies the relationship:

$$\left| Z - \frac{(Q_{sh} + Q_{DMA}) \cdot ln\left(\frac{R_{out}}{R_{in}}\right)}{2\pi L \cdot |V_{DMA}|} \right| \le \pm \Delta Z \tag{1}.$$

The HR-DMA is operated in a closed loop with a recirculating sheath flow rate  $Q_{sh} = 140$  slpm crossing the classification section to achieve a nominal filtering resolution  $\frac{\Delta Z}{Z} = \frac{Q_{sh}}{Q_{DMA}} > 20$ , with a triangular transfer function established for materials whose Brownian diffusion in the classification section is negligible (Knutson and Whitby 1975; Stolzenburg and McMurry 2008; Flagan 1999, 2011). One can estimate that the used HR-DMA settings make Brownian losses and the decay in resolution (i.e., the broadening of the transfer function) negligible for Z at least up to 0.61 cm<sup>2</sup>s<sup>-1</sup>V<sup>-1</sup> (i.e.,  $D_{DMA}$ at least as small as 1.85 nm). The HR-DMA flow rates are monitored with dedicated (3% accurate) mass flow meters.  $V_{DMA}$  is stepped from  $-5 \,\mathrm{kV}$  to  $+5 \,\mathrm{kV}$  using a high voltage power supply (model HP5, Applied Kilvot) controlled by a digital Data AcQuisition (DAQ) system (model PCIe-6353, National Instuments Inc.) and inhouse developed LabView program. The relation between Z and  $V_{DMA}$  in Equation (1) is refined by performing direct calibrations using Tetra-heptyl-ammonium monomer cations (THA+) which have known electrical mobility in air  $Z_{THA+}=0.9709 \,\mathrm{cm}^2\mathrm{s}^{-1}\mathrm{V}^{-1}$  at room temperature (Ude and Fernandez de La Mora 2005). During the mobility calibrations, THA + is seeded in the dilution nitrogen by electrospraying a 100 μmol solution of THA-Bromide in Ethanol (Carbone, Attoui, and Gomez 2016) so that one can measure the HR-DMA voltage,  $V_{DMA}$  $_{THA+}$ , filtering the THA + ion.

The mobility diameter,  $D_{DMA}$ , of any material classified by the HR-DMA can be calculated from its electrical mobility by solving implicitly the Stokes Millikan relation (Larriba-Andaluz and Carbone 2021). Since the materials classified in this study are smaller than 10 nm, one can assume they carry one elementary charge (Wiedensohler 1988; Hoppel and Frick 1986; Carbone, Attoui, and Gomez 2016;



Carbone et al. 2019) and use a simplified approximate relationship valid in the free molecular regime (Carbone, Attoui, and Gomez 2016):

$$D_{DMA} = D_{DMA-THA+} \sqrt{\frac{Z_{THA+}}{Z_{DMA}}} = D_{DMA-THA+} \sqrt{\frac{V_{DMA}}{V_{THA+}}}$$
(2)

Equation (2) relies on the literature estimate of  $D_{DMA-THA+}$ =1.47 nm performed in air at room temperature (Ude and Fernandez de La Mora 2005) to directly determine  $D_{DMA}$  with 3% accuracy (Carbone, Attoui, and Gomez 2016).

## 2.3. Particle counting

The aerosol classified by the HR-DMA is split using a Swagelok Tee connected to the inlet port of the WCPC directly and to the FCE through a 127 mm long static dissipative tube with ID = 6.35 mm (Static Dissipative PU Tubing, Freelin Wade). Repetitions of the experiments with the Tee connected to the HR-DMA, FCE, and WCPC in the three different possible orientations yielded the same results. The flow through the FCE is monitored with a calibrated flow sensor (Sensirion AG, SFM4100) and kept constant at  $Q_{FCE} = 5.7$  slpm. The FCE resistance,  $R_{FCE} = 1.0 \cdot 10^{12} \Omega$ , converts the current generated by the charged aerosol crossing the FCE to a voltage  $V_{FCE}$  (Fernandez de la Mora et al. 2017) which is acquired by the DAQ and saved by the LabView program as a function of  $D_{DMA}$ .  $V_{FCE}$  is readily converted to the number concentration of charges in the center of the Tee upon calculating the penetration efficiency,  $P_{FCE}$  ( $D_{DMA}$ ), through the connection between the Tee and the FCE, by using established relationships for diffusion losses in tubes (Hinds 1999; Friedlander 2000; Kumar et al. 2008):

$$n_{FCE}(D_{DMA}) = \frac{V_{FC}(D_{DMA})}{e \cdot R_{FCE} \cdot Q_{FCE}} \cdot \frac{1}{P_{FCE}(D_{DMA})}$$
(3).

The remaining fraction of the HR-DMA-classified aerosol is processed by the WCPC from where it is extracted with a constant  $Q_{CPC}$  flow rate. The flow extracted from the Tee by the WCPC crosses a short connection before entering the cylindrical growth tube within the water-wetted wick where water supersaturation is created by controlling the wick temperature in three sequential stages. The three stages are built of 42.93 mm, 12.70 mm, and 53.85 mm long aluminum blocks perforated to be crossed by a continuous tubular (4.76 mm ID and 6.35 mm OD) water-wetted wick. The stages' blocks are separated by 2.5 mm thick insulators and either heated by cartridge heaters or cooled by Peltier elements.

In this study, the temperature of the first water stage, the "conditioner," is kept constant at  $T_{conditioner} = 1$  °C. The temperature of the second water stage, the "initiator" stage, T<sub>initiator</sub>, was set between 40 °C and 99 °C. The temperature difference between the conditioner and initiator determines the maximum water vapor supersaturation and hence controls the mobility diameter of the materials that are detected with 50% efficiency,  $d_{50\%}$ . In all measurements, the temperature of the third "moderator" stage, T<sub>moderator</sub>, is also set to 1°C but its actual value increases when increasing T<sub>initiator</sub> above 50 °C because of the limited power supplied to the cooling element of the WCPC prototype. Table 1 lists the actual values of T<sub>conditioner</sub> and T<sub>moderator</sub> for all investigated values of T<sub>initiator</sub>.

The droplets exiting the growth tube are counted through the number of pulses,  $N_{CPC}$ , generated by the WCPC optical counter over a time interval of  $\Delta t_{CPC}$  = 0.5 s. The counts are digitally acquired and saved by the DAQ and the LabView program as a function of  $D_{DMA}$ . A correction to account for coincidence counting errors (Collins, Dick, and Romay 2013; Enroth et al. 2018; Hering, Lewis, and Spielman 2020; Avula et al. 2021) is applied in all measurements, although it is negligible in most cases thanks to the small values of  $N_{CPC}$  measured when using high dilutions and HR-DMA resolutions. The number concentration of the materials detected by the CPC as a function of  $D_{DMA}$  is easily inferred using established relationships for diffusion losses in the connection between the Tee and the WCPC (Hinds 1999; Friedlander 2000; Kumar et al. 2008):

$$n_{CPC}(D_{DMA}) = \frac{N_{CPC}(D_{DMA})}{\Delta t_{CPC} \cdot Q_{CPC}} \cdot \frac{1}{P_{CPC}(D_{DMA})}$$
(4).

efficiency of the Efficiency<sub>CPC</sub>, is readily inferred by normalizing the number concentration of the charged materials it detects over the total measured by the FCE:

$$Efficiency_{CPC}(D_{DMA}) = \frac{n_{CPC}(D_{DMA})}{n_{FCE}(D_{DMA})} \tag{5}.$$

## 2.3.1. DEG saturator inlet

Significant subsets of measurements are performed upon installing the DEG saturator inlet immediately

**Table 1.** Tested operating temperatures of the WCPC.

T <sub>initiator</sub> , °C	$T_{conditioner},{}^{\circ}C$	T <sub>moderator</sub> , °C
40	1	1
70	1	2
80	1	5
90	1	6
99	1	9

upstream of the WCPC, as depicted in Figure 1. In traditional DEG-nButonal CPCs, there is a hot DEG "saturator" followed by a cold "condenser." The smallest detectable size is limited by the maximum temperature difference between the saturator and the condenser that can be maintained without causing homogeneous nucleation of the DEG vapor. In the system under test, the first cold water "conditioner" stage, acts as the DEG "condenser." The two DEG stages are built of 50.8 mm and 25.4 mm aluminum blocks perforated to be crossed by a tubular (9.53 mm OD and 4.76 mm ID) wick whose walls are wetted by DEG. The blocks are separated by a 2.5 mm thick insulator and are heated with independently controlled cartridge heaters. The flow extracted from the Tee crosses a short connection before entering the cylindrical region within the wick wetted by DEG whose temperature is adjusted in two sequential stages, to achieve the control of both the DEG vapor concentration and flow temperature at the inlet of the WCPC.

The ability to control the flow temperature and DEG vapor concentration with two separate stages enables the highest DEG supersaturation to be established at a given  $T_{initiator}$  while preventing homogenous nucleation. This is achieved by operating the second stage at a temperature  $T_{\rm DEG2}$  lower than that of the first stage,  $T_{\rm DEG1}$ , both in the interval between 30 °C and 55 °C. Experimentally, we investigated the set of DEG-WCPC temperatures listed in Table 2, all of which avoid DEG homogeneous nucleation.

# 2.3.2. Penetration efficiencies

The operating conditions are chosen to keep laminar flow (Re < 2300) from the HR-DMA to the FCE and the CPC and the penetration efficiencies are calculated as (Kumar et al. 2008):

$$P_{FCE/CPC} = 1 - 5.5\beta^{\frac{2}{3}} + 3.77\beta$$
 if  $\beta < 0.009$  (6a)

$$P_{FCE/CPC} = 0.819 - 5.5e^{-11.5\beta} + 0.975e^{-70.1\beta}$$
 if  $\beta > 0.009$  (6b).

In Equations (6a) and (6b),  $\beta$  is a dimensionless deposition parameter defined as  $\beta(D_{DMA}) = l \cdot Z(D_{DMA}) \cdot k_B T/(e \cdot Q_{FCE/CPC})$  where l is the length of the tube,  $k_B T$  is the Boltzmann factor at T=298 K, e is the elementary charge, and  $Q_{FCE/CPC}$  is the aerosol flow rate in connections of the Tee to the detection devices (either FCE, WCPC, or DEG-WCPC). The top panel of Figure 2 shows the penetration efficiency as a function of  $D_{DMA}$  calculated for the connections

**Table 2.** Operating temperatures tested with the DEG saturator inlet coupled to the WCPC.

Saturator $T_{DEG}$ , °C	WCPC <i>T<sub>H2O</sub>,</i> °C
$T_{DEG1}/T_{DEG2}$	$T_{conditioner}/T_{initiator}/T_{moderator}$
30/30	1/90/6
40/40	1/70/2
55/35	1/40/1

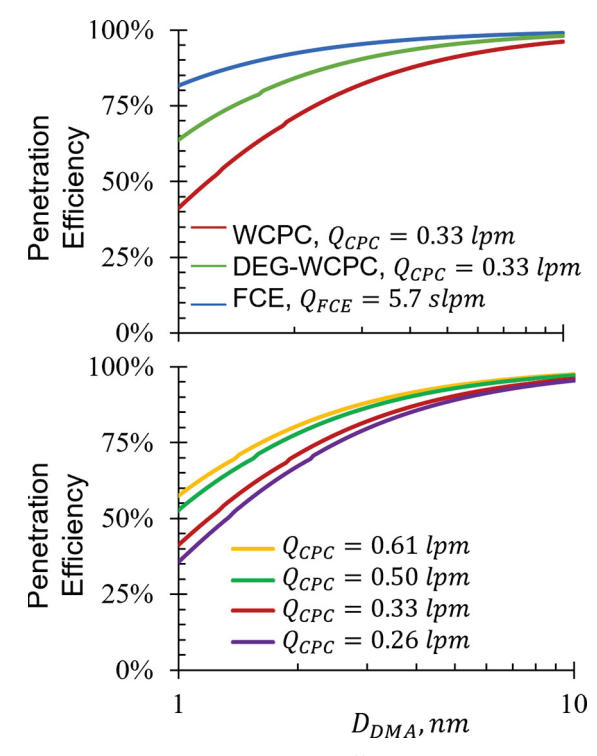


**Figure 2.** (Top panel) Penetration efficiency in the connections between the Tee and the WCPC, DEG-WCPC, and the FCE as a function of  $D_{DMA}$ , under typical operating conditions with  $Q_{CPC} = 0.33$  lpm and  $Q_{FCE} = 5.7$  slpm. (Bottom panel) Penetration through the WCPC inlet tube operated with different values of  $Q_{CPC}$  (see legend).

from the Tee to either the FCE, the WCPC, or the DEG-WCPC, operated with their typical flowrates  $Q_{CPC}=0.33$  lpm and  $Q_{FCE}=5.7$  slpm. The bottom panel of Figure 2 shows the penetration efficiency through the WCPC connection for several  $Q_{CPC}$ s from 0.26 lpm to 0.61 lpm. The lengths used in the penetration efficiency calculations are listed in Table 3 and include the inlet ports of either the FCE, the WCPC, or the DEG saturator inlet, as well as the dead volume within the Tee connector.

# 2.5. COMSOL multiphysics model

A 2D axisymmetric CFD model of the flow within the WCPC and DEG saturator inlet is implemented using COMSOL Multiphysics (version 6.1, COMSOL Inc.) based on previous work of our group (Carbone,

Table 3. Lengths of the connections used in the penetration efficiency calculation.

From the Tee's center to:	I, mm
Faraday Cup Electrometer (FCE)	127 48
DEG saturator inlet	38

Cattaneo, and Gomez 2015). The model leverages the weakly compressible (Ma < 0.3) laminar flow, the heat transfer in fluid, the transport of concentrated species, and the chemistry modules of COMSOL to account for the temperature dependence of transport phenomena with a mixture-averaged approach (Kee, Warnatz, and Miller 1983). The Lennard-Jones potential characteristic distance, well depth, and the dipole moment of nitrogen and water vapor molecules are taken from the literature (Ranzi et al. 2012) whereas they are estimated for DEG based on the molecule structure and functional groups (Hirschfelder, Curtiss, and Bird 1964). The polynomial interpolation parameters of the species' thermodynamic properties are imported from the Burcat's thermodynamic database (Burcat and Ruscic 2005).

The model is based on first principles, accounts for the gravitational force, and considers the cylinders (i.e., the connection and the interior of the DEG-wet wick if the DEG saturator is installed, and the connection and the interior of the water-wet wick) crossed sequentially by the flow in addition to the conical nozzle accelerating it toward the counting optics (Hering et al. 2019). The computational domain is divided into approximately 300,000 elements with the mesh being refined in the proximity of solid walls (i.e., of wicks, connections, and nozzle) to resolve the boundary layers. We verified that the mesh used herein is finer than what is necessary to obtain mesh-independent results. As boundary conditions, plug flow of pure nitrogen at ambient temperature is assigned at the inlet of the first connection, zero velocity and zero diffusive flows are assigned at connections and nozzle walls, and uniform pressure (965 mbar as in all experiments) and zero gradients of all other variables at the nozzle outlet. At the DEG and WCPC wicks' walls, dedicated boundary conditions are implemented based on the assigned stages' temperatures (as set in the experiments and listed in Tables 1 and 2). The concentrations of water and DEG at the wick walls are assigned to be either zero (for water at the DEG wick and for DEG at the water wick) or equal to the value determined by the appropriate Antoine equations for either water (NIST Chemistry WebBook 2023) or DEG (MEGlobal 2023). The non-zero normal (Stefan) velocity due to vaporization and condensation of DEG and Water at the wick walls is calculated implicitly to balance the diffusive flow

of nitrogen to the wall since its total flow through the wick must be zero at any location (i.e., because of the nitrogen mass balance). Condensation of water and DEG on the aerosol to be detected is not accounted for in the model since we verified that the mass flow of the droplets is negligible compared to the mass flow of their vapors at the WCPC outlet, in all investigated conditions (i.e., heterogenous condensation does not affect the concentration fields of the condensing vapors). The fields of water and DEG supersaturations are determined by using the same Antoine equations to calculate the saturation pressure,  $p_{sab}$  based on the local temperature. The fields of the local Kelvin critical diameter for condensation of water and DEG are inferred as  $D_{Kelvin} = \frac{4\gamma V_m}{RT} \cdot \ln \left( \frac{p_{sat}}{p} \right)$ (Friedlander 2000; Seinfeld and Pandis 2016), based on the molar volume,  $V_{mv}$  of the condensing fluids as well as their surface tension,  $\gamma$ , calculated at the local temperature. To account for the effect of the electrostatic energy of singly charged condensing nuclei, a refined Thomson-Kelvin critical diameter is calculated by numerically solving the relationship (Thomson 1903; Seto et al. 1997; Winkler et al. 2008):

$$D_{Thomson-Kelvin} = D_{Kelvin} \cdot \left[ 1 - \frac{e^2(1 - 1/\varepsilon)}{8\pi^2 \gamma \varepsilon_0 \cdot D_{Thomson-Kelvin}^3} \right]$$
(7).

Equation (7) accounts for the vacuum dielectric constant,  $\varepsilon_0$ , and the condensation nuclei single elementary charge, e, as well as the relative dielectric constant,  $\varepsilon$ , and surface tension,  $\gamma$ , of the condensing fluid. One should note that the Thomson-Kelvin thermodynamic theories may yield increasingly inaccurate results at increasing larger supersaturations causing extremely small  $D_{Kelvin}$ and  $D_{Thomson-Kelvin}$  values. This is the case because properties, such as  $\gamma$  and  $\varepsilon$ , may change in value and even lose meaning for portions of matter approaching that of a few molecules. Additionally, they may be affected by the presence of an electric charge and by the chemical affinity of vapor molecules and the condensation nuclei materials (e.g., the surface tension of a pure liquid is different from that of the same liquid solvating an impurity).

#### 3. Results and discussion

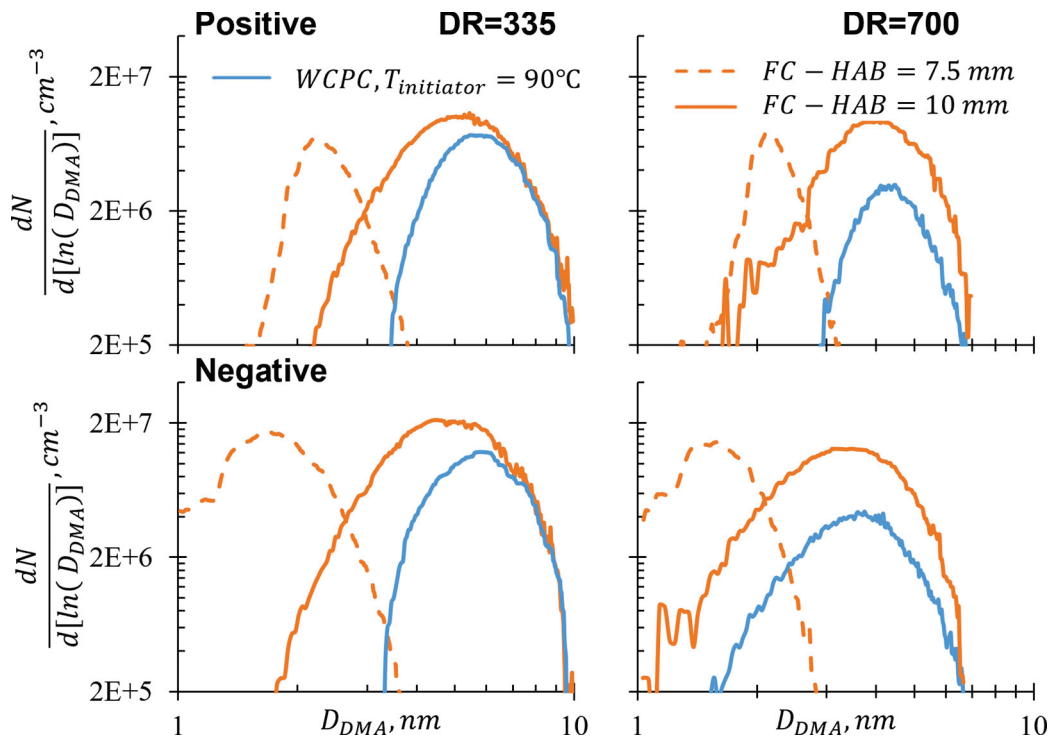
# 3.1. Size distribution functions of naturally charged carbonaceous flame products

Figure 3 shows the Size Distribution Functions (SDFs) of naturally charged carbonaceous materials within the flame as measured after being extracted at either  $HAB = 7.5 \, \text{mm}$  or  $HAB = 10 \, \text{mm}$  with either the  $0.36 \,\mathrm{mm}$  (DR = 335 in the left panels) or the  $0.25 \,\mathrm{mm}$  (DR = 700 in the right panels) orifice probe. The orange lines consider all charged materials counted by the FCE and contrast their SDFs to that of the fraction detectable by the WCPC when it is operated with  $T_{initiator} = 90$  °C and  $Q_{CPC} = 0.33$  lpm, shown with blue lines. The top and bottom panels of Figure 3 show the results for materials carrying either a positive or a negative charge, respectively. Consistent with literature results (Carbone, Attoui, and Gomez 2016), at  $HAB = 7.5 \, mm$  all charged carbonaceous materials sampled from the flame have  $D_{DMA}$  smaller than 3 nm which are too small to be detected by the WCPC even with the high supersaturations implemented using a large  $T_{initiator} = 90$  °C and small  $T_{conditioner} = 1$  °C. naturally charged carbonaceous materials extracted at HAB = 10 mm encompass a broader dimensional range extending up to 10 nm after coagulation in the probe at the lowest dilution. Their SDFs are slightly different in opposite polarities as already reported in the literature (Carbone, Attoui, and Gomez 2016) and the WCPC can detect an increasingly larger fraction of them when  $D_{DMA}$  increases above 3 nm. From  $D_{DMA}$  larger than 7 nm the SDFs measured by the FCE and WCPC become almost identical, indicating that the WCPC detection efficiency approaches 100%.

# 3.2. Modeled flow within the WCPC (without the DEG saturator inlet)

Figure 4 shows the results of the 2D axisymmetric COMSOL Multiphysics model with  $T_{initiator} = 90 \,^{\circ}\text{C}$ and  $Q_{CPC} = 0.33$  lpm. The left panel of Figure 4 depicts qualitatively the model results with a colormap of the water vapor saturation ratio established in the cylindrical region within the WCPC's water-wet wick. A maximum saturation ratio of approximately 7.5 is established by the initiator whereas a secondary supersaturated region, with values between 4 and 5.5, is generated by the downstream moderator as a result of cooling. The right panels of Figure 4 reports systematically the advection time history of temperature, saturation ratio, and the resulting Kelvin critical diameter,  $D_{Kelvin}$ , for water condensation established within the device. The history is tracked along six streamlines radially equispaced (but the axial one) in the inlet tube (ID = 3.96 mm) upstream of the WCPC wick. The origin of the advection time is set to zero when water vapor saturation is established first along each streamline.

The fields of temperature and water saturation ratio are not uniform within the WCPC but, interestingly, the device keeps  $D_{Kelvin}$  constant around 1.2 nm for more than 90 ms along any of the considered



**Figure 3.** Size Distribution Functions of carbonaceous materials naturally charged within the flame in either positive (top panels) or negative (bottom panels) polarity as measured after being diluted in nitrogen using Dilution Ratios (DRs) of either 335 (left) or 700 (right). Orange lines include all charged materials, counted by the FCE, whereas the blue lines include only that detectable by the WCPC operated with  $T_{initiator} = 90$  °C (see Table 1) and  $Q_{CPC} = 0.33$  lpm.

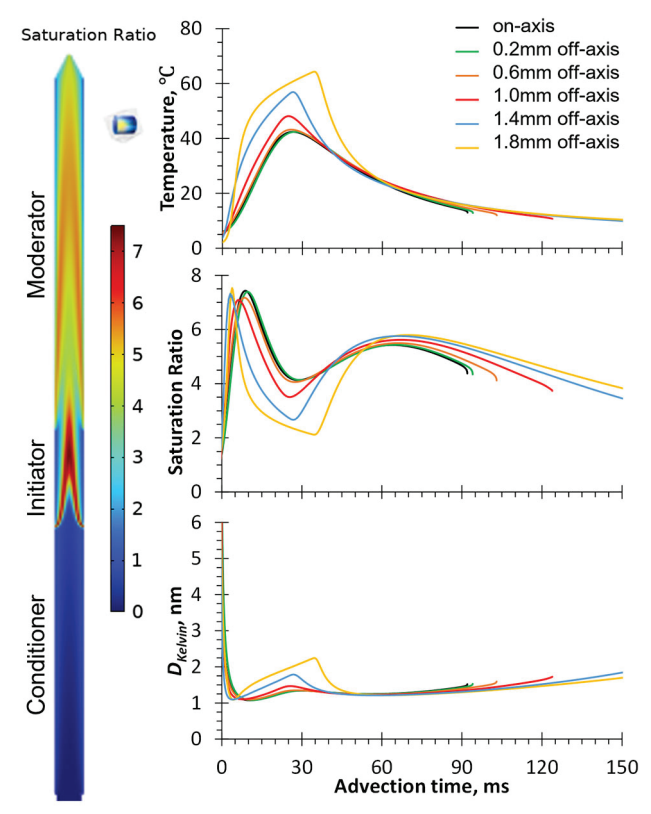


Figure 4. Results of the COMSOL model of the WCPC operated with  $T_{initiator} = 90$  °C (see Table 1) and  $Q_{CPC} = 0.33$  lpm. The 2D axisymmetric flow is depicted with the colormap of the water vapor saturation ratio within the water wick (left panel). The right panels show the profiles of Temperature, water saturation ratio, and critical Kelvin diameter as a function of the advection time along several streamlines originating at different equispaced off-axis positions (see legend) within the inlet tube (ID = 3.96 mm) preceding the water wick.

streamlines, including that within 0.2 mm from the inlet tube and water wick walls. Therefore, the WCPC has the potential to activate condensation growth and enable the detection of materials as small as 1.2 nm when they are hydrophilic (i.e., water wettable) and one would expect the detection efficiency to increase sharply from zero to 100% as a function of  $D_{DMA}$ right before such a threshold (Fernandez de la Mora 2011). Instead, since carbonaceous flame products are hydrophobic, the water condensation growth is activated at  $D_{DMA}$  significantly larger than  $D_{Kelvin}$ , as apparent in Figure 3.

Similar qualitative results are obtained when modeling the WCPC operated with different T<sub>initiator</sub> but the same  $Q_{CPC} = 0.33$  lpm. Of course, the computed minimum values of  $D_{Kelvin}$  are very sensitive to the used T<sub>initiator</sub> and approximately equal to 1.0 nm,  $1.2 \,\mathrm{nm}, \ 1.6 \,\mathrm{nm}, \ \text{and} \ 4.5 \,\mathrm{nm} \ \text{when} \ T_{\mathrm{initiator}}$  is set to 99 °C, 90 °C, 70 °C, and 40 °C, respectively. The model also enables us to compute the net flow rate of water vaporized within the WCPC which exits it as a vapor contributing to a fraction of  $Q_{CPC} = 0.33$  lpm extracted at the WCPC outlet (as opposed to the DEG flow at the WCPC outlet which is negligible in all investigated conditions). The flow rate of water vapor exiting the WCPC is also sensitive to T<sub>initiator</sub> and T<sub>moderator</sub>, and is computed to be 85 cm<sup>3</sup>/min, 23 cm<sup>3</sup>/min, 8 cm<sup>3</sup>/min, and 3 cm<sup>3</sup>/min when T<sub>initiator</sub> is set to 99 °C, 90 °C, 70 °C, and 40 °C, respectively. This means that the flow at the WCPC inlet is smaller than  $Q_{CPC}$  and their difference increases with increasing T<sub>initiator</sub>. The small difference is accounted for in the results to obtain a refined estimate of the penetration efficiency within the connection between the Tee and the WCPC.

# 3.3. WCPC detection efficiency and optimized

The  $D_{DMA}$ -dependent detection efficiency of the WCPC can be calculated with Equations (3)–(5) from the results of the type presented in Figure 3. To obtain results with a good signal-to-noise ratio in the entire sub-10 nm  $D_{DMA}$  interval, we overlapped the results of several measurements performed with two different DRs at HAB = 10 mm. The overlapping not only highlights the very small uncertainty of the experimental results but also reveals that the WCPC detection efficiency is unaffected by the coagulation of the naturally charged flame products occurring at low temperatures in the sampling probe (Carbone, Attoui, and Gomez 2016; Carbone et al. 2019). Therefore, coagulation in the probe does not modify the water wettability of the naturally charged flame products. Since  $Q_{CPC}$  is an important parameter affecting the WCPC detection efficiency, Figure 3 shows the results when the WCPC is operated with  $T_{initiator} = 90$  °C and different  $Q_{CPC}$ . The optimal flow rate is a tradeoff between minimizing the diffusive losses in the growth tube and allowing enough time at near-maximum water supersaturation to activate and complete the condensation growth of the materials to be detected. Figure 5 demonstrates that  $Q_{CPC} = 0.33$  lpm is an optimal operating value to detect the smallest possible naturally charged flame-formed materials with the tested WCPC operated with  $T_{initiator} = 90$  °C.

# 3.4. Sigmoid fitting of the WCPC detection efficiency at different initiator temperatures

Figure 6 shows the detection efficiency of flameformed carbonaceous materials naturally charged in

either positive (top panel) or negative (bottom panel) polarity. The plots overlap symbols including the results of several measurements performed with two different DRs at HAB = 10 mm obtained by operating the WCPC with  $Q_{CPC} = 0.33$  lpm and different values of T<sub>initiator</sub> between 70 °C and 99 °C, right at the onset of water boiling. The lower limit of 70°C was set by the necessity to detect at least a fraction of the naturally charged flame-formed carbonaceous materials with  $D_{DMA}$  smaller than 10 nm whose SDF is depicted in Figure 3. The horizontal dashed line in Figures 5 and 6 highlights the 50% detection cutoff mobility diameter,  $d_{50\%}$ , which is positioned at approximately 9 nm when  $T_{initiator} = 70$  °C. Increasingly larger values of T<sub>initiator</sub> enable the WCPC to activate the condensation growth and detection of naturally charged carbonaceous flame materials with progressively smaller  $D_{DMA}$  since  $d_{50\%}$  shifts down to approximately 4.5 nm when  $T_{initiator} = 99 \,^{\circ}\text{C}$ . Table 4 summarizes the experimental results by listing the accurate values of  $d_{50\%}$  observed in the measurements with different values of  $T_{initiator}$  but constant  $Q_{CPC} = 0.33$  lpm. Results highlight a slight but systematic polarity dependency of the WCPC in detecting naturally charged carbonaceous flame products smaller than 10 nm, with condensation growth and detection of positively charged

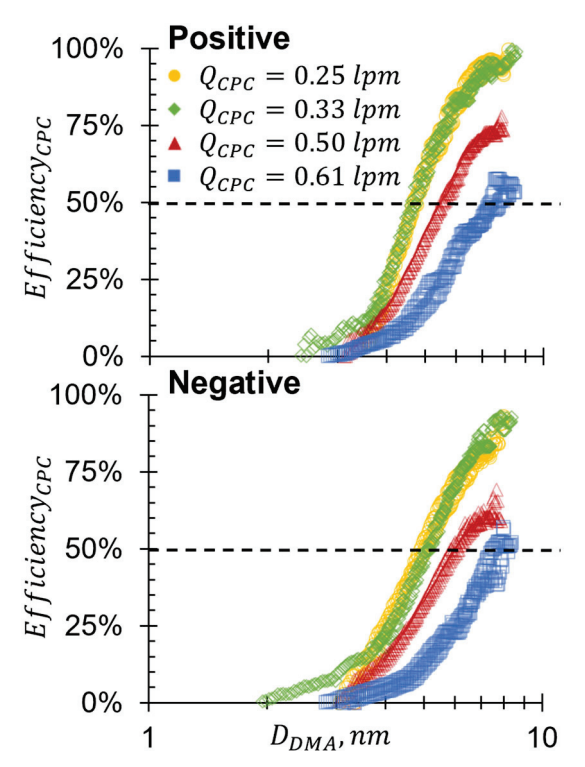


Figure 5. Detection efficiency of flame-formed carbonaceous materials naturally charged in either positive (top panel) or negative (bottom panel) polarity when the WCPC is operated with  $T_{initiator} = 90$  °C (see Table 1) and extracting different  $Q_{CPC}$  at its outlet (see legend).

materials being activated at smaller  $D_{DMA}$  compared to negatively charged ones. Therefore, flame-formed carbonaceous materials naturally charged in positive polarity are slightly less hydrophobic than negatively charged ones. Regardless of hydrophobicity, flame materials naturally charged in positive polarity have been observed to be more prone to growth compared to negatively charged ones (Carbone, Attoui, and Gomez 2016; Carbone et al. 2019).

The detection efficiency of the WCPC can be fit by Logarithmic Sigmoid Functions (LSFs) which are also included as lines in Figure 6. The LSF uses two parameters and follows the functional expression:

$$LSF = \frac{1}{1 + e^{-\alpha \ln\left(\frac{D_{DMA}}{d_{50\%}}\right)}} = \frac{1}{1 + \left(\frac{D_{DMA}}{d_{50\%}}\right)^{-\alpha}} \tag{8}.$$

In Equation (8),  $D_{DMA}$  is the independent variable,  $d_{50\%}$  is the 50% detection cutoff diameter identified in Figure 6 and listed in Table 4, and  $\alpha$  is a steepness

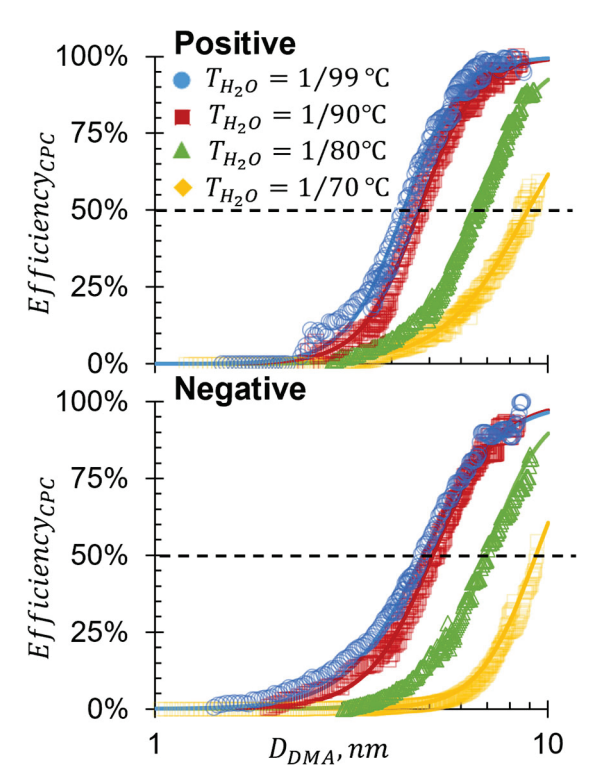


Figure 6. Detection efficiency of flame-formed carbonaceous materials naturally charged in either positive (top panel) or negative (bottom panel) polarity when the WCPC is operated  $Q_{CPC} =$ 0.33 lpm and different  $T_{initiator}$  (see legend and Table 1).

Table 4. Parameters of the logarithmic sigmoid function of Equation (6) fitting the WCPC experimental results of Figure 6.

T <sub>H₂O</sub> , °C	<b>d</b> <sub>50%</sub> , nm	$\alpha^+$	<b>d</b> _ <sub>50%</sub> , nm	$\alpha^{-}$
1/70	9.0	N/A	9.3	N/A
1/80	6.6	6.0	7.0	6.0
1/90	4.6	6.0	5.1	5.2
1/99	4.3	6.0	4.8	4.5



factor utilized to fit the experimental results whose values are also summarized in Table 4. The larger the  $\alpha$  value the sharper the increase of the measured detection efficiency with increasing  $D_{DMA}$ . Since the changes in Gibbs free energy driving heterogeneous nucleation (Thomson 1903; Fletcher 1958; Friedlander 2000; Fernandez de la Mora 2011; Seinfeld and Pandis 2016) are affected by both the water-wettability and the shape/morphology of the condensation nuclei,  $\alpha$ accounts for both the polydispersity relative to these parameters of naturally charged flame materials with the same  $D_{DMA}$ , as well as in the supersaturation-time history experienced along different streamlines within the WCPC, which Figure 4 shows to be minimal. Therefore, the WCPC experimental results summarized in Table 4 suggest that flame materials with a negative natural charge are not only overall less hydrophilic than that with a positive charge but also have a progressively broader polydispersity in activating water condensation (e.g., in shape and wettability) below 5-6 nm. Indeed, when one enables the detection of smaller flame materials by using a larger  $T_{initiator}$ ,  $\alpha$ decreases noticeably for those carrying a natural negative charge but does not for that carrying a posi-

Finally, the maximum slope,  $\frac{1}{\Delta D_{DMA}} = \frac{d(LSF)}{d(D_{DMA})}|_{max}$ , of the LSF fitting quantifies the ability to distinguish particles with different  $D_{DMA}$ s by adjusting the WCPC operating parameters (Riipinen et al. 2009; Winkler and Wagner 2022). The (approximately linear) correspondence between the  $\alpha$  steepness factor of the detection efficiency and the potential size resolution of the WCPC measurements (Attoui et al. 2023) is listed in Table 5.

# 3.5. Model results of the WCPC with the DEG saturator inlet

An enhancement of the WCPC performance in detecting hydrophobic combustion-generated carbonaceous material can be achieved by installing the DEG saturator inlet upstream of the WCPC. The device establishes near saturation of the DEG vapor before the aerosol enters the cold WCPC conditioner where high DEG supersaturations are established to activate the heterogeneous condensation on the materials to be detected. Subsequently, water condensation on the just-formed DEG nanodroplets can easily take place since DEG is completely miscible with (i.e., wettable by) water (MEGlobal 2023).

The effect of installing the DEG saturator inlet is depicted in the left panels of Figure 7 showing

**Table 5.** Relation between the steepness factor,  $\alpha$ , of the logarithmic sigmoid fitting function and the size resolving power (Attoui et al. 2023),  $d_{50\%}/\Delta D_{DMA}$ , of the width,  $\Delta D_{DMA}$ , of the WCPC detection efficiency.

α	2.0	3.0	4.0	5.0	6.0
$d_{50\%}/\Delta D_{DMA}$	0.65	0.84	1.06	1.30	1.54

colormaps of the DEG saturation ratio field within the WCPC water wick, as computed by the COMSOL model for the three investigated operating conditions. In all cases, DEG saturation achieves its maximum value downstream the cold WCPC initiator with values of approximately 10 and over 50 when the DEG saturator inlet is operated at the lowest,  $T_{DEG}$  = 30/30 °C, and highest,  $T_{DEG} = 55/35$  °C, investigated DEG temperatures, respectively. The heating provided by the WCPC initiator lowers temporarily the DEG saturation while establishing water supersaturation whereas both DEG and water supersaturation are reboosted in the downstream cold moderator. For a quantitative comparison of the computational results, the right panels of Figure 7 report the profiles of temperature and saturation ratio and  $D_{Thomson-Kelvin}$  of both DEG (solid line) and water (dashed line) vapors along the WCPC axial streamline. As in Figure 4, the profiles in the right panels of Figure 7 are plotted as a function of the advection time which is set equal to zero when the DEG vapor saturation ratio equals 2. Figure 7 does not depict the variability of the histories along different off-axis streamlines because we want to highlight the effects of the DEG-WCPC operating temperatures. Additionally, the advection histories along different streamlines are quite similar to each other with the most noticeable difference being caused by the stretching of the profiles toward longer advection times along streamlines at increasingly larger offaxis positions and closer to the walls, similar to what is depicted in Figure 4 for the WCPC alone. Importantly, the minimum values of the DEG and water  $D_{Thomson-Kelvin}$  are almost the same along any streamline but for those in very close proximity to the inlet tube/wick wall (i.e., the DEG  $D_{Thomson-Kelvin}$ increases less than 15% or 25% compared to its onaxis value when considering the streamlines displaced 0.38 mm or 0.18 mm from the walls, respectively).

A closer inspection of Figure 7 reveals that the highest DEG supersaturation (solid lines) is established right upstream of and overlaps with the water vapor supersaturated region (dashed lines). For any given setting, the DEG  $D_{Thomson-Kelvin}$  is kept near its minimum value for at least approximately 20 ms. During this time, DEG wettable materials larger than the DEG  $D_{Thomson-Kelvin}$  should grow via DEG

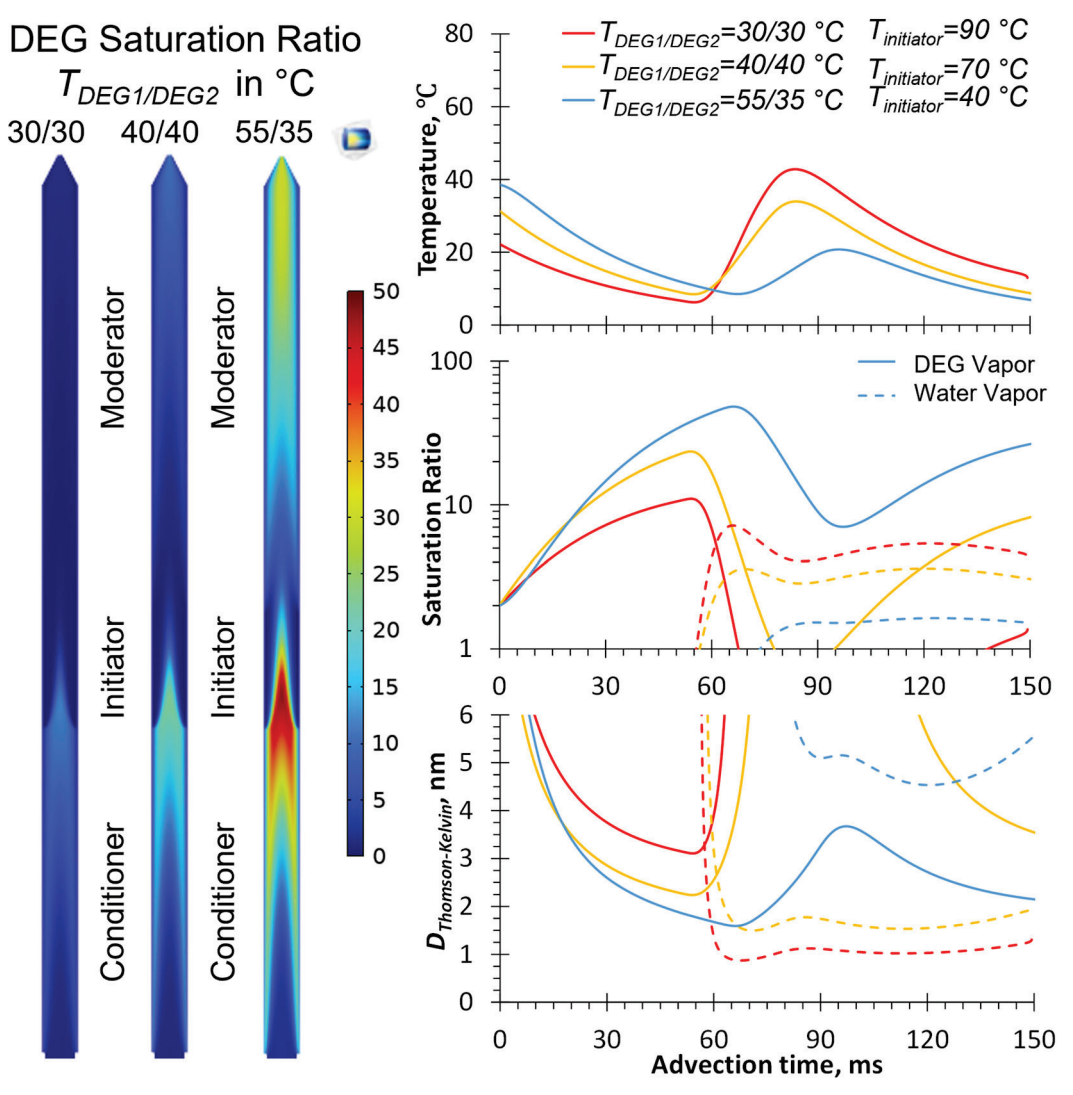


**Figure 7.** COMSOL model of the WCPC operated with  $Q_{CPC} = 0.33$  lpm upon installing the DEG saturator inlet and using three  $T_{DEG}$  and  $T_{H2O}$  settings (see legend and Table 2). The left panels show 2D colormaps of the DEG vapor saturation ratio and the right panels the axial profiles of temperature and saturation ratio and critical Thomson-Kelvin diameter of DEG (solid lines) and water (dashed lines) vapor as a function of the advection residence time along the WCPC axial streamline.

condensation into droplets able to activate water condensation in the ensuing water supersaturated region. Under all operating conditions, the device establishes simultaneous supersaturation of DEG and water for a few tens of milliseconds so that the growth can also be activated by two-component heterogeneous nucleation (Seinfeld and Pandis 2016). The maximum DEG saturation ratio increases approximately from 10 up to 65 as  $T_{DEG}$  is raised from 30/30 °C to 55/35 °C. As a result, the minimum  $D_{Thomson-Kelvin}$  for DEG condensation is quantified to be approximately 3.2 nm, 2.2 nm, and 1.6 nm when the DEG inlet is operated with  $T_{DEG} = 30/30 \,^{\circ}\text{C}$ ,  $40/40 \,^{\circ}\text{C}$ , and  $55/35 \,^{\circ}\text{C}$ , respectively. Since DEG is completely mixable with water, the growth of the just-formed DEG droplets is expected to occur always given that  $D_{Thomson-Kelvin}$  for water condensation is smaller than 4.5 nm in all investigated conditions, as also shown in Figure 7. Consequently the  $d_{50\%}$  of the DEG-WCPC is mostly limited by the wettability of the materials to be detected by DEG. The ensuing experimental results assess the DEG wettability of flame-formed carbonaceous nanoparticles by comparing the experimentally observed  $d_{50\%}$  to the DEG critical diameters predicted by the model.

# 3.6. Detection efficiency of the DEG-WCPC

Figure 8 compares the results of experiments performed with and without the DEG saturator inlet operated at  $T_{DEG}=30/30\,^{\circ}\mathrm{C}$  installed at the inlet of the WCPC. The DEG saturator inlet enhances the detection efficiency of the WCPC and enables the partial detection of materials with  $D_{DMA}$  smaller than

3 nm, including that sampled from the flame at HAB = 7.5 mm, depicted in Figure 3. The detection efficiency as a function of  $D_{DMA}$  is obtained by overlapping the results of several measurements performed at  $HAB = 7.5 \, mm$  and  $HAB = 10 \, mm$  in the flame and upon applying either DR= 335 or DR = 700. The smooth overlap quantifies the small uncertainty of the experimental results and demonstrates not only that the detection efficiency of the DEG-WCPC is unaffected by coagulation of the flame products at low temperatures in the sampling probe, (similar to what is observed in Figures 5 and 6 for the WCPC alone) but it is also marginally affected by the charge polarity and by aging and growth occurring at high temperatures in the flame. The polarity, probe coagulation, and flame growth/aging approximate independence of the results suggest that these phenomena affect minimally the DEG wettability of the naturally charged carbonaceous flame products. Additionally, the  $d_{50\%}$ from experiments with  $T_{DEG} = 30/30$  °C evidenced in Figure 8, matches the DEG  $D_{Thomson-Kelvin} = 3.2 \, \text{nm}$ predicted by the COMSOL model results in Figure 7. The matching indicates the complete wettability of the flame products by DEG so that the model may be

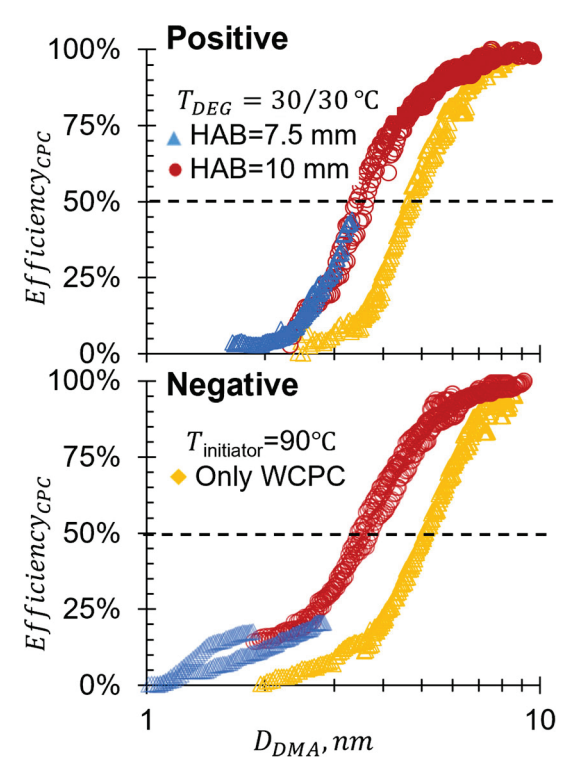


Figure 8. Efficiency of the WCPC ( $T_{initiator} = 90\,^{\circ}\text{C}$ ) with and without the DEG saturator inlet operated at  $T_{DEG} = 30/30\,^{\circ}C$ (see Table 2), in detecting carbonaceous materials naturally charged in either positive (top) or negative (bottom) polarities sampled from the flame at twoHAB (see legend) and with two different dilution ratios (DR = 335 or DR = 700).

able to predict  $d_{50\%}$  also in the other experimentally investigated conditions.

Therefore, one wants to examine experimentally the effect of increasing  $T_{DEG}$  on the detection efficiency of naturally charged flame-formed carbonaceous materials. As partially mentioned in the methods section, an increase in  $T_{DEG1}$  has to be accompanied by a reduction in  $T_{initiator}$  (and in one case of  $T_{DEG2}$ ) to control the supersaturation and temperature fields and avoid 2-components water-DEG homogeneous nucleation (Seinfeld and Pandis 2016). Figure 9 depicts the measured detection efficiency of the DEG-WCPC operated with  $T_{DEG}$  equal to 30/30 °C, 40/40 °C, and 55/35 °C. The increase of  $T_{\rm DEG1}$  boosts the downstream DEG supersaturation and enables the detection of ever smaller naturally charged flame-formed carbonaceous materials. Figure 9 shows also that the experimentally determined values of  $d_{50\%}$ , highlighted by the horizontal dashed line and listed in Table 6, are very close to the DEG D<sub>Thomson-Kelvin</sub> computed by our COMSOL model (see Figure 7). This is the case even if  $d_{50\%}$  is expressed as a mobility diameter (Larriba-Andaluz and Carbone 2021) whereas the  $D_{Thomson-Kelvin}$  is a volume/surface equivalent diameter obtained under the assumption of a spherical shape for the condensation nuclei (Friedlander 2000; Seinfeld and Pandis 2016). A visual comparison of the consistency between computational and experimental results, regardless of the charge polarity and sample dilution ratio, is provided as the graphical abstract of this manuscript. The closeness of the experimental detection cutoff sizes and the computational  $D_{Thomson-Kelvin}$  supports the finding that naturally charged flame-formed carbonaceous materials are completely wettable by DEG and suggests that most of them have an approximately spherical shape. The fact that an increasingly larger fraction of materials with  $D_{DMA}$  smaller than  $d_{50\%}$  and  $D_{Thomson-Kelvin}$  is detected when increasing  $T_{DEG1}$  and detecting ever smaller materials, suggests a progressively increasing departure from the spherical shape for materials smaller than 2.5 nm, as expected since they are clusters of small aromatics (Carbone et al. 2019; Carbone, Gleason, and Gomez 2023). Other possibilities to explain the detection of materials smaller than D<sub>Thomson-Kelvin</sub> include the non-zero probability of condensation growth being activated under a finite free energy barrier over a finite time interval (Fletcher 1958; Fernandez de la Mora 2011), the presence of an increasing (but still small) fraction of doubly charged materials when their sizes decrease (Carbone et al. 2019), and 2-components DEG-water (heterogenous)

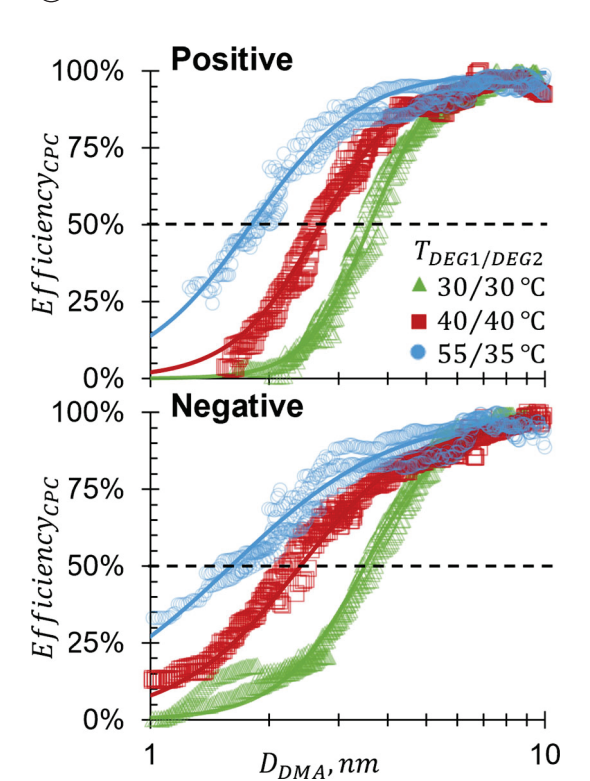


Figure 9. Detection efficiency of the DEG-WCPC operated under different temperature conditions (see legend and Table 2) as measured for flame-formed carbonaceous materials naturally charged in either positive (top) or negative (bottom) polarity. Symbols depict the experimental results and solid lines show their logarithmic sigmoid fittings (LSF).

Table 6. Parameters of the Logarithmic Sigmoid Function (LSF) fitting the detection efficiency of the DEG-WCPC measured for naturally charged flame-formed carbonaceous materials and shown in Figure 9.

	Positive Charge		Negative Charge		Any Charge	
$T_{DEG}$ , $^{\circ}$ C	<b>d</b> <sup>+</sup> <sub>50%</sub> , nm	$\alpha^+$	<b>d</b> <sup>-</sup> <sub>50%</sub> , nm	α-	<b>d</b> <sub>50%</sub> , nm	α
30/30	3.7	5.4	3.6	4.5	3.6	5.1
40/40	2.7	3.9	2.4	2.8	2.6	3.5
55/35	1.8	3.0	1.6	2.1	1.7	2.4

condensation (Winkler et al. 2011; Seinfeld and Pandis 2016) being activated at a critical diameter smaller than that of DEG alone in the zone where DEG and water supersaturation are established simultaneously (see Figure 7).

Figure 9 highlights also that the detection efficiency of the DEG-WCPC can be well fitted by the Logarithmic Sigmoid Function shown as solid lines in Figure 9. The values of  $d_{50\%}$  and steepness parameter, α, which allow for the best fitting of the experimental results in Figure 9 are listed in Table 6 which, therefore, provides a concise summary of the experimental results obtained with the DEG-WCPC. The fittings are performed either upon considering materials naturally charged in opposite polarities separately or upon lumping them together regardless of the charge polarity (as in the graphical abstract) given that the polarity affects only slightly the detection efficiency. Table 6 highlights such a small polarity dependence which may be related to different deviations for ions of opposite polarities of  $D_{DMA}$  (Larriba-Andaluz and Carbone 2021) from the surface/volume equivalent diameter which affects condensation (Thomson 1903; Fletcher 1958; Friedlander 2000; Seinfeld and Pandis 2016). One should note that the polarity dependence of the DEG-WCPC detection efficiency is small but opposite compared to that of the WCPC alone. Results reveal also that the lowering of  $d_{50\%}$  with increasing  $T_{DEG}$  is accompanied by a reduction in the steepness factor,  $\alpha$ , of the detection efficiency (i.e., an increase in width of the profiles as listed in Table 6), as also apparent in Figure 9. The reduction of the  $\alpha$ value is slightly more pronounced for materials carrying a negative rather than a positive charge and may be a consequence of an increasingly larger shape and/or charge number polydispersity of the naturally charged flame-formed carbonaceous materials with decreasing  $D_{DMA}$  smaller than 2.5 nm. A more pronounced polydispersity of materials with negative rather than positive charge may also explain the different α values observed for the smallest detected materials with charges of opposite polarity (consistent with the results of the WCPC alone summarized in Figure 6 and Table 4).

#### 4. Conclusion

This work focuses on characterizing the detection efficiency of a (DiEthylene Glycol enhanced-, DEG-) Water-based Condensation Particle Counter, WCPC, prototype (ADI-2021-01, Aerosol Dynamics Inc.) for naturally charged carbonaceous materials generated from an incipiently sooting laminar premixed flame. The effects of the WCPC operating parameters as well as that of the installation and operation of a DEG saturator inlet, converting the WCPC into the DEG-WCPC, are investigated experimentally. The experimental work is complemented by a first principles COMSOL Multiphysics 2D computational model of the flow within the WCPC and the DEG-WCPC. The major findings of the results follow below.

The WCPC can detect naturally charged flamegenerated carbonaceous materials with a mobility diameter smaller than 10 nm if operated with an initiator temperature, T<sub>initiator</sub>, above 70 °C while keeping the conditioner temperature at 1°C. An



increase in T<sub>initiator</sub> from 70 °C to 99 °C enhances the detection of the smallest materials shifting the 50% detection cutoff diameter,  $d_{50\%}$ , down to values at least as small as 4.5 nm.

- The WCPC detection efficiency is noticeably different for flame carbonaceous materials carrying natural charges of opposite polarities, with a lower detection efficiency of negatively compared to positively charged materials.
- The (DEG-) WCPC establishes a field of the Kelvin critical diameter which has approximately equal minimum values along different streamlines and the naturally charged flame-formed carbonaceous materials activate water condensation growth only when their sizes are much larger than that predicted by the Kelvin theory, as a result of their hydrophobic nature.
- The optimal WCPC flow rate is achieved by making a compromise between the minimization of diffusion losses and the achievement of relatively long advection times (of the order of 90 ms) in the supersaturated region of the device for water condensation to grow the naturally charged flame products into detectable droplets. The optimal flow rate is affected not only by the WCPC geometry but also by T<sub>initiator</sub> (when larger than 80 °C) and the water wettability of the materials to be detected.
- The installation of the DEG saturator inlet enhances the detection efficiency of the smallest flameformed naturally charged materials and circumvents the limitations related to their low water wettability so that the  $d_{50\%}$  can be lowered to approximately 1.6 nm.
- The measured  $d_{50\%}$  of the DEG-WCPC is predicted accurately by the COMSOL model as the critical Thomson-Kelvin diameter for DEG condensation, a fact indicating that naturally charged flameformed carbonaceous nanoparticles are completely wettable by DEG.
- Condensation growth and detection are observed for a fraction of the materials with sizes smaller than the DEG critical condensation Thomson-Kelvin diameter. This suggests that two-component condensation caused by the concurrent supersaturation of DEG and water vapors may be activated by materials smaller than those activated by DEG condensation alone. Shape and/or charge number polydispersity of naturally charged flame-formed carbonaceous materials with the same mobility diameter can also contribute to this effect. The polydispersity broadens for materials of decreasing

- mobility diameter and is more evident when their charge is negative rather than positive.
- The installation of the DEG saturator inlet minimizes (but inverts) the polarity sensitivity of the WCPC in detecting hydrophobic naturally charged carbonaceous flame products. Indeed, the DEG-WCPC detection efficiency is only slightly larger for negatively compared to positively charged materials, possibly as a result of their broader shape and/or charge number polydispersity.
- In all considered cases, the WCPC's detection efficiency as a function of the mobility diameter can be fitted with a Logarithmic Sigmoid Function (LS) parameterized with  $d_{50\%}$  and a steepness factor, which greatly simplifies the data inversion of any measurement results.

# **Acknowledgments**

This work acknowledges Chongai Kuang for the concept and initial development efforts of the DEG inlet, as part of the project PASCCALS (Process-level AdvancementS of Climate through Cloud and Aerosol Lifecycle Studies), funded by the Office of Biological and Environmental Research in the Department of Energy, Office of Science, and through the United States Department of Energy contract no. DE-SC0012704 to Brookhaven National Laboratory.

#### **Disclaimer**

Gregory S. Lewis and Arantza Eiguren-Fernandez declare to be shareholders of Aerosol Dynamics Inc. which designed, manufactured, and owns the tested ADI-2021-1 WCPC prototype.

## **Funding**

Financial support for this work is being provided by the USA National Science Foundation (Grant#CBET- 2013382, Prof. Harsha K. Chelliah serving as Program Manager).

#### **ORCID**

Francesco Carbone http://orcid.org/0000-0003-3991-

### References

Ahonen, L. R., J. Kangasluoma, J. Lammi, K. Lehtipalo, K. Hämeri, T. Petäjä, and M. Kulmala. 2017. First measurements of the number size distribution of 1-2 nm aerosol particles released from manufacturing processes in a cleanroom environment. Aerosol Sci. Technol. 51 (6):685-93. doi:10.1080/02786826.2017.1292347.

- Attoui, M. 2018. Activation of sub 2 nm singly charged particles with butanol vapors in a boosted 3776 TSI CPC. J. *Aerosol Sci.* 126:47–57. doi:10.1016/j.jaerosci.2018.08.005.
- Attoui, M., L. J. Perez-Lorenzo, C. A. Brock, and J. Fernandez de la Mora. 2023. High resolution characterization of a sheathed axisymmetric variable supersaturation condensation particle sizer. J. Aerosol Sci. 169: 106112. doi:10.1016/j.jaerosci.2022.106112.
- Avula, S., R. Remiarz, G. J. Chancellor, T. Anderson, D. C. Bjorkquist, R. Caldow, S. Morrel, F. R. Quant, S. V. Hering, and G. S. Lewis. 2021. Condensation particle counter false count performance, US Patent 10914667B2, filed October 25, 2019, and issued February 9, 2021.
- Barmpounis, K., A. Ranjithkumar, A. Schmidt-Ott, M. Attoui, and G. Biskos. 2018. Enhancing the detection efficiency of condensation particle counters for sub-2 nm particles. J. Aerosol Sci. 117:44-53. doi:10.1016/j.jaerosci.2017.12.005.
- Basile, G., A. Rolando, A. D'Alessio, A. D'Anna, and P. Minutolo. 2002. Coagulation and carbonization processes in slightly sooting premixed flames. Proc. Combust. Inst. 29 (2):2391-7. doi:10.1016/S1540-7489(02)80291-7.
- Bockhorn, H., A. D'Anna, and A. F. Sarofim. 2009. Combustion generated fine carbonaceous particles. Edited by H. Wang. Universitätsverlag Karlsruhe. Karlsruhe: KIT Scientific. doi:10.5445/KSP/1000013744.
- Brilke, S., J. Resch, M. Leiminger, G. Steiner, C. Tauber, P. J. Wlasits, and P. M. Winkler. 2020. Precision characterization of three ultrafine condensation particle counters using singly charged salt clusters in the 1-4 nm size range generated by a bipolar electrospray source. Aerosol Sci. Technol. 54 (4):396-409. doi:10.1080/02786826.2019.1708260.
- Burcat, A., and B. Ruscic. 2005. Third millenium ideal gas and condensed phase thermochemical database for combustion (with update from active thermochemical tables). Argonne, IL: Argonne National Lab. doi:10.2172/925269.
- Carbone, F., F. Cattaneo, and A. Gomez. 2015. Structure of incipiently sooting partially premixed ethylene counterflow flames. Combust. Flame 162 (11):4138-48. doi:10. 1016/j.combustflame.2015.08.008.
- Carbone, F., K. Gleason, and A. Gomez. 2017. Probing gasto-particle transition in a moderately sooting atmospheric pressure ethylene/air laminar premixed flame. Part I: Gas phase and soot ensemble characterization. Combust. Flame 181:315-28. doi:10.1016/j.combustflame.2017.01.029.
- Carbone, F., K. Gleason, and A. Gomez. 2023. Soot research: Relevance and priorities by mid-century. In Combustion chemistry and the carbon neutral future. 1st ed., ed. K. Brezinsky. Cambridge, MA: Elsevier. doi:10. 1016/B978-0-323-99213-8.00007-2.
- Carbone, F., M. Attoui, and A. Gomez. 2016. Challenges of measuring nascent soot in flames as evidenced by high-resolution differential mobility analysis. Aerosol Sci. Technol. 50 (7):740-57. doi:10.1080/02786826.2016.1179715.
- Carbone, F., M. R. Canagaratna, A. T. Lambe, J. T. Jayne, D. R. Worsnop, and A. Gomez. 2019. Exploratory analysis of a sooting premixed flame via on-line high resolution (APi-TOF) mass spectrometry. Proc. Combust. Inst. 37 (1):919-26. doi:10.1016/j.proci.2018.08.020.
- Carbone, F., M. R. Canagaratna, A. T. Lambe, J. T. Jayne, D. R. Worsnop, and A. Gomez. 2021. Detection of weakly bound clusters in incipiently sooting flames via ion seeded dilution and collision charging for (APi-TOF)

- mass spectrometry analysis. Fuel 289:119820. doi:10.1016/ j.fuel.2020.119820.
- Carbone, F., S. Moslih, and A. Gomez. 2017. Probing gas-toparticle transition in a moderately sooting atmospheric pressure ethylene/air laminar premixed flame. Part II: Molecular clusters and nascent soot particle size distributions. Combust. Flame 181:329-41. doi:10.1016/j.combustflame.2017.02.021.
- Cheng, Y. S. 2011. Condensation particle counters. In Aerosol measurement: Principles, techniques, and applications. 3rd ed., ed. P. Kulkarni, P. A. Baron, and K. Willeke, 381-92. Hoboken, NJ: John Wiley & Sons. doi: 10.1002/9781118001684.ch17.
- Collins, A. M., W. D. Dick, and F. J. Romay. 2013. A new coincidence correction method for condensation particle counters. Aerosol Sci. Technol. 47 (2):177-82. doi:10.1080/ 02786826.2012.737049.
- Commodo, M., K. Kaiser, G. De Falco, P. Minutolo, F. Schulz, A. D'Anna, and L. Gross. 2019. On the early stages of soot formation: molecular structure elucidation by highresolution atomic force microscopy. Combust. Flame 205: 154-64. doi:10.1016/j.combustflame.2019.03.042.
- D'Anna, A. 2009. Combustion-formed nanoparticles. Proc. Combust. Inst. 32 (1):593-613. doi:10.1016/j.proci.2008.09.005.
- Eiguren-Fernandez, A., N. Kreisberg, and S. V. Hering. 2017. An online monitor of the oxidative capacity of aerosols (o-MOCA). Atmos. Meas. Tech. 10 (2):633-44. doi:10.5194/amt-10-633-2017.
- Enroth, J., J. Kangasluoma, F. Korhonen, S. V. Hering, D. Picard, G. S. Lewis, M. Attoui, and T. Petäjä. 2018. On the time response determination of condensation particle counters. Aerosol Sci. Technol. 52 (7):778-87. doi:10.1080/ 02786826.2018.1460458.
- Fernandez de la Mora, J. 2011. Heterogeneous nucleation with finite activation energy and perfect wetting: Capillary theory versus experiments with nanometer particles, and extrapolations on the smallest detectable nucleus. Aerosol Sci. Technol. 45 (4):543-54. doi:10.1080/ 02786826.2010.550341.
- Fernandez de la Mora, J. 2017. Expanded flow rate range of high-resolution nanoDMAs via improved sample flow injection at the aerosol inlet slit. J. Aerosol Sci. 113:265-75. doi:10.1016/j.jaerosci.2017.07.020.
- Fernandez de la Mora, J., and J. Kozlowski. 2013. Hand-held differential mobility analyzers of high resolution for 1-30 nm particles: Design and fabrication considerations. *J. Aerosol Sci.* 57:45–53. doi:10.1016/j.jaerosci.2012.10.009.
- Fernandez de la Mora, J., L. J. Perez-Lorenzo, G. Arranz, M. Amo-Gonzalez, and H. Burtscher. 2017. Fast highresolution nanoDMA measurements with a 25 ms response time electrometer. Aerosol Sci. Technol. 51 (6): 724-34. doi:10.1080/02786826.2017.1296928.
- Flagan, R. C. 1999. On differential mobility analyzer resolution. Aerosol Sci. Technol. 30 (6):556-70. doi:10.1080/ 027868299304417.
- Flagan, R. C. 2011. Electrical mobility methods for submicrometer particle characterization. In Aerosol measurement: Principles, techniques, and applications. 3rd ed., ed. P. Kulkarni, P. A. Baron, and K. Willeke, 339-64. Hoboken, NJ: John Wiley & Sons, Inc. doi:10.1002/9781118001684.ch15.
- Flagan, R. C., S. L. Kaufman, and G. J. Sem. 2005. Particle surface treatment for promoting condensation. Patent No. US7407531B2.



- Fletcher, N. H. 1958. Size effect in heterogeneous nucleation. The Journal of Chemical Physics 29 (3):572-6. doi: 10.1063/1.1744540.
- Friedlander, S. K. 2000. Smoke, dust, and haze: Fundamentals of aerosol dynamics. 2nd ed. New York: Oxford University Press.
- Gamero-Castaño, M., and J. Fernandez de La Mora. 2000. A condensation nucleus counter (CNC) sensitive to singly charged sub-nanometer particles. J. Aerosol Sci. 31 (7):757-72. doi:10.1016/S0021-8502(99)00555-8.
- Hering, S. V., and M. R. Stolzenburg. 2005. A method for particle size amplification by water condensation in a laminar, thermally diffusive flow. Aerosol Sci. Technol. 39 (5):428-36. doi:10.1080/027868290953416.
- Hering, S. V., G. S. Lewis, and S. R. Spielman. 2020. Particle surface treatment for promoting condensation. Patent No. US20200408931A1.
- Hering, S. V., G. S. Lewis, S. R. Spielman, A. Eiguren-Fernandez, N. M. Kreisberg, C. Kuang, and M. Attoui. 2017. Detection near 1-nm with a laminar-flow, waterbased condensation particle counter. Aerosol Sci. Technol. 51 (3):354-62. doi:10.1080/02786826.2016.1262531.
- Hering, S. V., G. S. Lewis, S. R. Spielman, and A. Eiguren-Fernandez. 2019. A MAGIC concept for self-sustained, water-based, ultrafine particle counting. Aerosol Sci. Technol. 53 (1):63–72. doi:10.1080/02786826.2018.1538549.
- Hering, S. V., S. R. Spielman, and G. S. Lewis. 2014. Moderated, water-based, condensational particle growth in a laminar flow. Aerosol Sci. Technol. 48 (4):401-8. doi: 10.1080/02786826.2014.881460.
- Hewitt, R. E., H. F. Chappell, and J. J. Powell. 2020. Small and dangerous? Potential toxicity mechanisms of common exposure particles and nanoparticles. Curr. Opin. Toxicol. 19:93-8. doi:10.1016/j.cotox.2020.01.006.
- Hinds, W. C. 1999. Aerosol technology—properties, behavior and measurement of airborne particles. 2nd ed. New York: John Willey & Sons.
- Hirschfelder, J. O., C. F. Curtiss, and R. B. Bird. 1964. Molecular theory of gases and liquids (appendix, table 1c). New York: John Willey & Sons.
- Hoppel, W. A., and G. M. Frick. 1986. Ion—aerosol attachment coefficients and the steady-state charge distribution on aerosols in a bipolar ion environment. J. Aerosol Sci. 5 (1):1-21. doi:10.1080/02786828608959073.
- Iida, K., M. R. Stolzenburg, and P. H. McMurry. 2009. Effect of working fluid on sub-2 nm particle detection with a laminar flow ultrafine condensation particle counter. Aerosol Sci. Technol. 43 (1):81-96. doi:10.1080/02786820802488194.
- Iida, K., M. R. Stolzenburg, P. H. McMurry, J. N. Smith, F. R. Quant, D. R. Oberreit, P. B. Keady, A. Eiguren-Fernandez, G. S. Lewis, N. M. Kreisberg, et al. 2008. An ultrafine, water-based condensation particle counter and its evaluation under field conditions. Aerosol Sci. Technol. 42 (10):862-71. doi:10.1080/02786820802339579.
- Jiang, J., M. Chen, C. Kuang, M. Attoui, and P. H. McMurry. 2011. Electrical mobility spectrometer using a diethylene glycol condensation particle counter for measurement of aerosol size distributions down to 1 nm. Aerosol Sci. Technol. 45 (4):510-21. doi:10.1080/02786826. 2010.547538.
- Johansson, K. O., M. P. Head-Gordon, P. E. Schrader, K. R. Wilson, and H. A. Michelsen. 2018. Resonance-stabilized

- hydrocarbon-radical chain reactions may explain soot inception and growth. Science 361 (6406):997-1000. doi: 10.1126/science.aat3417.
- Kangasluoma, J., and M. Attoui. 2019. Review of sub-3 nm condensation particle counters, calibrations, and cluster generation methods. Aerosol Sci. Technol. 53 (11):1277-310. doi:10.1080/02786826.2019.1654084.
- Kangasluoma, J., C. Kuang, D. Wimmer, M. P. Rissanen, K. Lehtipalo, M. Ehn, D. R. Worsnop, J. Wang, M. Kulmala, and T. Petäjä. 2014. Sub-3 nm particle size and composition dependent response of a nano-CPC battery. Atmos. Meas. Tech. 7 (3):689-700. doi:10.5194/amt-7-689-2014.
- Kee, R. J., J. Warnatz, and J. A. Miller. 1983. A FORTRAN computer code package for the evaluation of gas-phase viscosities, conductivities, and diffusion coefficients. Sandia National Laboratories Report SAND86-8246, Livermore, CA.
- Knutson, E. O., and K. T. Whitby. 1975. Aerosol classification by electric mobility: Apparatus, theory, and applications. J. Aerosol Sci. 6 (6):443-51. doi:10.1016/0021-8502(75)90060-9.
- Kuang, C., M. Chen, P. H. McMurry, and J. Wang. 2012. Modification of laminar flow ultrafine condensation particle counters for the enhanced detection of 1 nm condensation nuclei. Aerosol Sci. Technol. 46 (3):309-15. doi: 10.1080/02786826.2011.626815.
- Kuldinow, D., A. Przybylak, L. J. Perez Lorenzo, D. Oberreit, and J. Fernandez de la Mora. 2022. Cluster activation studies with a diffusive condensation particle counter: Effect of chemical composition. J. Aerosol Sci. 161:105917. doi:10.1016/j.jaerosci.2021.105917.
- Kulkarni, P., P. A. Baron, and K. Willeke. 2011. Aerosol measurement: Principles, techniques, and applications. 3rd ed. Hoboken, NJ: John Willey & Sons.
- Kumar, P., P. Fennell, J. Symonds, and R. Britter. 2008. Treatment of losses of ultrafine aerosol particles in long sampling tubes during ambient measurements. Atmos. Environ. 42 (38):8819-26. doi:10.1016/j.atmosenv. 2008.09.003.
- Larriba-Andaluz, C., and F. Carbone. 2021. The size-mobility relationship of ions, aerosols, and other charged particle matter. J. Aerosol Sci. 151:105659. doi:10.1016/j. jaerosci.2020.105659.
- Lehtipalo, K., J. Kontkanen, J. Kangasluoma, A. Franchin, D. Wimmer, S. Schobesberger, H. Junninen, T. Petäjä, M. Sipilä, and D. Worsnop. 2014. Methods for determining particle size distribution and growth rates between 1 and 3 nm using the Particle Size Magnifier. Boreal Environ. Res. 19:215-236.
- Lewis, G. S., and S. V. Hering. 2013. Minimizing concentration effects in water-based, laminar-flow condensation particle counters. Aerosol Sci. Technol. 47 (6):645-54. doi: 10.1080/02786826.2013.779629.
- Lighty, J. S., J. M. Veranth, and A. F. Sarofim. 2000. Combustion aerosols: Factors governing their size and composition and implications to human health. J. Air Waste Manag. Assoc. 50 (9):1565-618. doi:10.1080/ 10473289.2000.10464197.
- Manisalidis, I., E. Stavropoulou, A. Stavropoulos, and E. Bezirtzoglou. 2020. Environmental and health impacts of air pollution: A review. Front. Public Health. 8:14. doi:10. 3389/fpubh.2020.00014.

- McMurry, P. H. 2000. The history of condensation nucleus counters. Aerosol Sci. Technol. 33 (4):297-322. doi:10. 1080/02786820050121512.
- MEGlobal. 2023. Diethylene glycol. https://www.meglobal.biz/ wp-content/uploads/2022/05/DEG\_Guide\_Rev\_2022\_W6.pdf.
- Moreno-Ríos, A. L., L. P. Tejeda-Benítez, and C. F. Bustillo-Lecompte. 2022. Sources, characteristics, toxicity, and control of ultrafine particles: An overview. Geosci. Front. 13 (1):101147. doi:10.1016/j.gsf.2021.101147.
- Nel, A., T. Xia, L. Mädler, and N. Li. 2006. Toxic potential of materials at the nanolevel. Science 311 (5761):622-7. doi:10.1126/science.1114397.
- NIST Chemistry WebBook. 2023. https://webbook.nist.gov/ chemistry/.
- Oberdörster, G., E. Oberdörster, and J. Oberdörster. 2005. Nanotoxicology: An emerging discipline evolving from studies of ultrafine particles. Environ. Health Perspect. 113 (7):823-39. doi:10.1289/ehp.7339.
- Pedata, P., T. Stoeger, R. Zimmermann, A. Peters, G. Oberdörster, and A. D'Anna. 2015. Are we forgetting the smallest, sub 10 nm combustion generated particles? Part. Fibre Toxicol. 12 (1):34. doi:10.1186/s12989-015-0107-3.
- Picard, D., M. Attoui, and K. Sellegri. 2019. B3010: A boosted TSI 3010 condensation particle counter for airborne studies. Atmos. Meas. Tech. 12 (4):2531-43. doi:10. 5194/amt-12-2531-2019.
- Ranzi, E., A. Frassoldati, R. Grana, A. Cuoci, T. Faravelli, A. P. Kelley, and C. K. Law. 2012. Hierarchical and comparative kinetic modeling of laminar flame speeds of hydrocarbon and oxygenated fuels. Prog. Energy Combust. Sci. 38 (4):468-501. doi:10.1016/j.pecs.2012.03.004.
- Riipinen, I., H. E. Manninen, T. Yli-Juuti, M. Boy, M. Sipilä, M. Ehn, H. Junninen, T. Petäjä, and M. Kulmala. 2009. Applying the condensation particle counter battery (CPCB) to study the water-affinity of freshly-formed 2-9nm particles in boreal forest. Atmos. Chem. Phys. 9 (10): 3317-30. doi:10.5194/acp-9-3317-2009.
- Rönkkö, T., and H. Timonen. 2019. Overview of sources and characteristics of nanoparticles in urban traffic-influenced areas. J. Alzheimers. Dis. 72 (1):15-28. doi:10.3233/JAD-190170.
- Rundel, J. A., C. M. Thomas, P. E. Schrader, K. R. Wilson, K. O. Johansson, R. P. Bambha, and H. A. Michelsen. 2022. Promotion of particle formation by resonance-stabilized radicals during hydrocarbon pyrolysis. Combust. Flame 243: 111942. doi:10.1016/j.combustflame.2021.111942.
- Schraufnagel, D. E. 2020. The health effects of ultrafine particles. Exp. Mol. Med. 52 (3):311-7. doi:10.1038/s12276-020-0403-3.
- Schulz, F., M. Commodo, K. Kaiser, G. De Falco, P. Minutolo, G. Meyer, A. D'Anna, and L. Gross. 2019. Insights into incipient soot formation by atomic force microscopy. Proc. Combust. Inst. 37 (1):885-92. doi:10. 1016/j.proci.2018.06.100.
- Seinfeld, J. H., and S. N. Pandis. 2016. Atmospheric chemistry and physics: From air pollution to climate change. 3rd ed. New York: John Wiley & Sons.
- Seto, T., K. Okuyama, L. de Juan, and J. Fernandez de la Mora. 1997. Condensation of supersaturated vapors on monovalent and divalent ions of varying size. J. Chem. Phys. 107 (5):1576-85. doi:10.1063/1.474510.

- Sgro, L., and J. Fernandez de la Mora. 2004. A simple turbulent mixing CNC for charged particle detection down to 1.2 nm. Aerosol Sci. Technol. 38 (1):1-11. doi:10.1080/ 02786820300982.
- Sharma, G., M. Wang, M. Attoui, X. You, and P. Biswas. 2021. Measurement of sub-3 nm flame-generated particles using butanol CPCs in boosted conditions. Aerosol Sci. Technol. 55 (7):785–94. doi:10.1080/02786826.2021.1896675.
- Sipilä, M., K. Lehtipalo, M. Kulmala, T. Petäjä, H. Junninen, P. P. Aalto, H. E. Manninen, E.-M. Kyrö, E. Asmi, I. Riipinen, et al. 2008. Applicability of condensation particle counters to measure atmospheric clusters. Atmos. Chem. Phys. 8 (14):4049-60. doi:10.5194/acp-8-4049-2008.
- Smyth, K. C., J. H. Miller, R. C. Dorfman, W. G. Mallard, and R. J. Santoro. 1985. Soot inception in a methane/air diffusion flame as characterized by detailed species profiles. Combust. Flame 62 (2):157-81. doi:10.1016/0010-2180(85)90143-9.
- Stolzenburg, M. R., and P. H. McMurry. 2008. Equations governing single and tandem DMA configurations and a new lognormal approximation to the transfer function. I. Aerosol Sci. 42 (6):421-32. doi:10.1080/02786820802157823.
- Thomson, J. J. 1903. Conduction of electricity through gases. New York: Cambridge University Press.
- TSI application note CPC-002 (A4). 2023. https://tsi.com/ getmedia/aed04052-5056-4fa4-b586-d648f1bb5262/CPC-002-appnote-A4?ext=.pdf
- Ude, S., and J. Fernandez de La Mora. 2005. Molecular monodisperse mobility and mass standards from electrosprays of tetra-alkyl ammonium halides. J. Aerosol Sci. 36 (10):1224–37. doi:10.1016/j.jaerosci.2005.02.009.
- Vanhanen, J., J. Mikkilä, K. Lehtipalo, M. Sipilä, H. E. Manninen, E. Siivola, T. Petäjä, and M. Kulmala. 2011. Particle size magnifier for nano-CN detection. Aerosol Sci. Technol. 45 (4):533-42. doi:10.1080/02786826.2010.547889.
- Wang, H. 2011. Formation of nascent soot and other condensed-phase materials in flames. Proc. Combust. Inst. 33 (1):41–67. doi:10.1016/j.proci.2010.09.009.
- Wiedensohler, A. 1988. An approximation of the bipolar charge distribution for particles in the submicron size range. J. Aerosol Sci. 19 (3):387-9. doi:10.1016/0021-8502(88)90278-9.
- Winkler, P. M., and P. E. Wagner. 2022. Characterization techniques for heterogeneous nucleation from the gas phase. J. Aerosol Sci. 159:105875. doi:10.1016/j.jaerosci.2021.105875.
- Winkler, P. M., G. Steiner, A. Vrtala, G. P. Reischl, M. Kulmala, and P. E. Wagner. 2011. Unary and binary heterogeneous nucleation of organic vapors on monodisperse WOx seed particles with diameters down to 1.4 nm. Aerosol Sci. Technol. 45 (4):493-8. doi:10.1080/02786826.2010.547536.
- Winkler, P. M., G. Steiner, A. Vrtala, H. Vehkamäki, M. Noppel, K. E. J. Lehtinen, G. P. Reischl, P. E. Wagner, and M. Kulmala. 2008. Heterogeneous nucleation experiments bridging the scale from molecular ion clusters to nanoparticles. Science 319 (5868):1374-7. doi:10.1126/science.1149034.
- Wlasits, P. J., D. Stolzenburg, C. Tauber, S. Brilke, S. H. Schmitt, P. M. Winkler, and D. Wimmer. 2020. Counting on chemistry: laboratory evaluation of seed-materialdependent detection efficiencies of ultrafine condensation particle counters. Atmos. Meas. Tech. 13 (7):3787-98. doi: 10.5194/amt-13-3787-2020.